

Nonlocal Gilbert damping tensor within the torque-torque correlation model

Danny Thonig,^{1,*} Yaroslav Kvashnin,¹ Olle Eriksson,^{1,2} and Manuel Pereiro¹

¹*Department of Physics and Astronomy, Materials Theory, Uppsala University, SE-75120 Uppsala, Sweden*

²*School of Science and Technology, Örebro University, SE-701 82 Örebro, Sweden*



(Received 29 September 2017; published 3 January 2018)

An essential property of magnetic devices is the relaxation rate in magnetic switching, which depends strongly on the damping in the magnetization dynamics. It was recently measured that damping depends on the magnetic texture and, consequently, is a nonlocal quantity. The damping enters the Landau-Lifshitz-Gilbert equation as the phenomenological Gilbert damping parameter α , which does not, in a straightforward formulation, account for nonlocality. Efforts were spent recently to obtain Gilbert damping from first principles for magnons of wave vector \mathbf{q} . However, to the best of our knowledge, there is no report about real-space nonlocal Gilbert damping α_{ij} . Here, a torque-torque correlation model based on a tight-binding approach is applied to the bulk elemental itinerant magnets and it predicts significant off-site Gilbert damping contributions, which could be also negative. Supported by atomistic magnetization dynamics simulations, we reveal the importance of the nonlocal Gilbert damping in atomistic magnetization dynamics. This study gives a deeper understanding of the dynamics of the magnetic moments and dissipation processes in real magnetic materials. Ways of manipulating nonlocal damping are explored, either by temperature, materials doping, or strain.

DOI: [10.1103/PhysRevMaterials.2.013801](https://doi.org/10.1103/PhysRevMaterials.2.013801)

I. INTRODUCTION

Efficient spintronics applications call for magnetic materials with low-energy dissipation when moving magnetic textures, e.g., in race track memories [1], skyrmion logics [2,3], spin logics [4], spin-torque nano-oscillator for neural network applications [5], or, more recently, soliton devices [6]. In particular, the dynamics of such magnetic textures—magnetic domain walls, magnetic skyrmions, or magnetic solitons—is well described in terms of precession and damping of the magnetic moment \mathbf{m}_i as it is formulated in the atomistic Landau-Lifshitz-Gilbert (LLG) equation for site i :

$$\frac{\partial \mathbf{m}_i}{\partial t} = \mathbf{m}_i \times \left(-\gamma \mathbf{B}_i^{\text{eff}} + \frac{\alpha}{m_s} \frac{\partial \mathbf{m}_i}{\partial t} \right), \quad (1)$$

where γ and m_s are the gyromagnetic ratio and the magnetic moment length, respectively. The precession field $\mathbf{B}_i^{\text{eff}}$ is of quantum mechanical origin and is obtained either from effective spin-Hamilton models [7] or from first principles [8]. In turn, energy dissipation is dominated by the *ad hoc* motivated viscous damping in the equation of motion scaled by the Gilbert damping tensor α . Commonly, the Gilbert damping is used as a scalar parameter in magnetization dynamics simulations based on the LLG equation. Strong efforts were spent in the last decade to put the Gilbert damping to a first-principles ground derived for collinear magnetization configurations. Different methods were proposed, e.g., the breathing Fermi surface [9–11], the torque-torque correlation [12], spin-pumping [13], or a linear response model [14,15]. Within a certain accuracy, the theoretical models allow to interpret [16] and reproduce experimental trends [17–20].

Depending on the model, deep insight into the fundamental electronic-structure mechanism of the Gilbert damping α is provided; damping is a Fermi-surface effect and depending on, e.g., scattering rate, damping occurs due to spin flip but also spin-conservative transition within a degenerated (intra-band but also interband transitions) and between nondegenerated (interband transitions) electron bands. As a consequence of these considerations, the Gilbert damping is proportional to the density of states, but it also scales with spin-orbit coupling [21,22]. The scattering rate Γ for the spin-flip transitions is allocated to thermal, but also correlation effects, making the Gilbert damping strongly temperature dependent, which must be a consideration when applying a three-temperature model for the thermal baths, say phonon [14], electron, and spin temperature [23]. In particular, damping is often related to the dynamics of a collective precession mode (macrospin approach) driven from an external perturbation field, as it is used in ferromagnetic resonance experiments (FMR) [24]. It is also established that the Gilbert damping depends on the orientation of the macrospin [25] and is, in addition, frequency dependent [26].

More recently, the role of noncollective modes to the Gilbert damping has been debated. Fähnle *et al.* [27] suggested to consider damping in a tensorial and nonisotropic form via α_i that differs for different sites i and depends on the whole magnetic configuration of the system. As a result, the experimentally and theoretically assumed local Gilbert equation is replaced by a nonlocal equation via nonlocal Gilbert damping α_{ij} accounting for the most general form of Rayleigh's dissipation function [28]. The proof of principles was given for magnetic domain walls [29,30], linking explicitly the Gilbert damping to the gradients in the magnetic spin texture $\nabla \mathbf{m}$. Even on a nanoscale level, the wave-number-dependent and, thus, nonlocal dissipation was measured recently by Li *et al.* [31] for

*danny.thonig@physics.uu.se

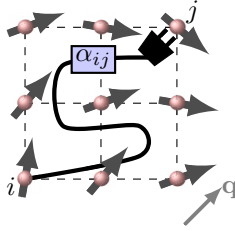


FIG. 1. Schematic illustration of nonlocal energy dissipation α_{ij} between site i and j (red balls) represented by a power cord in a system with spin wave (gray arrows) propagation \mathbf{q} .

25–200-nm-thick NiFe, Co, and CoFeB films using perpendicular spin wave resonance up to 26GHz. Such spatial nonlocality, in particular, for discrete atomistic models, allows further to motivate energy dissipation between two magnetic moments at sites i and j , and is represented by α_{ij} , as schematically illustrated in Fig. 1. An analytical expression for α_{ij} was already proposed by various authors [14,32,33], however, not much work has been done on a material specific, first-principles description of the atomistic nonlocal Gilbert damping α_{ij} . An exception is the work by Gilmore *et al.* [33] who studied $\alpha(\mathbf{q})$ in the reciprocal space as a function of the magnon wave vector \mathbf{q} and concluded that the nonlocal damping is negligible. Yan *et al.* [29] and Hals *et al.* [34], on the other hand, applied scattering theory according to Brataas *et al.* [35] to simulate noncollinearity in Gilbert damping, only in reciprocal space or continuous mesoscopic scale. Here we come up with a technical description of nonlocality of the damping parameter α_{ij} , in real space, and provide numerical examples for elemental, itinerant magnets, which might be of high importance in the context of ultrafast demagnetization [36].

The paper is organized as follows. In Sec. II, we introduce our first-principles model formalism based on the torque-torque correlation model to study nonlocal damping. This is applied to bulk itinerant magnets bcc Fe, fcc Co, and fcc Ni in both reciprocal and real space and it is analyzed in details in Sec. III. Here, we will also apply atomistic magnetization dynamics to outline the importance in the evolution of magnetic systems. Finally, in the last section, we conclude the paper by giving an outlook of our work.

II. METHODS

We consider the torque-torque correlation model introduced by Kamberský [10] and further elaborated on by Gilmore *et al.* [12]. Here, finite magnetic moment rotations couple to the Bloch eigenenergies $\varepsilon_{n,\mathbf{k}}$ and eigenstates $|n\mathbf{k}\rangle$, characterized by the band index n at wave vector \mathbf{k} , due to spin-orbit coupling. This generates a nonequilibrium population state (a particle-hole pair), where the excited states relax towards the equilibrium distribution (Fermi-Dirac statistics) within the time $\tau_{n,\mathbf{k}} = 1/\Gamma$, which we assume is independent of n and \mathbf{k} . In the adiabatic limit, this perturbation is described by the Kubo-Greenwood perturbation theory and in a nonlocal formulation reads [12,37]

$$\alpha^{\mu\nu}(\mathbf{q}) = \frac{g\pi}{m_s} \int_{\Omega} \sum_{nm} T_{nk;mk+q}^{\mu} (T_{nk;mk+q}^{\nu})^* W_{nk;mk+q} d\mathbf{k}. \quad (2)$$

Here, the integral runs over the whole Brillouin zone volume Ω . A frozen magnon of wave vector \mathbf{q} is considered that is ascribed to the nonlocality of α . The scattering events depend on the spectral overlap $W_{nk;mk+q} = \int \eta(\varepsilon) A_{nk}(\varepsilon, \Gamma) A_{mk+q}(\varepsilon, \Gamma) d\varepsilon$ between two bands $\varepsilon_{n,\mathbf{k}}$ and $\varepsilon_{m,\mathbf{k}+\mathbf{q}}$, where the spectral width of the electronic bands A_{nk} is approximated by a Lorentzian of width Γ . Note that Γ is a parameter in our model and can be spin-dependent as proposed in Ref. [38]. In other studies, this parameter is allocated to the self-energy of the system and is obtained by introducing disorder, e.g., in an alloy or alloy analogy model using the coherent potential approximation [14] (CPA) or via the inclusion of electron correlation [39]. Thus a principle study of the nonlocal damping versus Γ can be also seen as, e.g., a temperature-dependent study of the nonlocal damping. $\eta = \partial f / \partial \varepsilon$ is the derivative of the Fermi-Dirac distribution f with respect to the energy. $T_{nk;mk+q}^{\mu} = \langle n\mathbf{k} | \hat{T}^{\mu} | m\mathbf{k} + \mathbf{q} \rangle$, where $\mu = x, y, z$, are the matrix elements of the torque operator $\hat{T} = [\boldsymbol{\sigma}, \mathcal{H}_{\text{so}}]$ obtained from variation of the magnetic moment around certain rotation axis \mathbf{e} . $\boldsymbol{\sigma}$ and \mathcal{H}_{so} are the Pauli matrices and the spin-orbit Hamiltonian, respectively. In the collinear ferromagnetic limit, $\mathbf{e} = \mathbf{e}_z$ and variations occur in x and y , only, which allows to consider just one component of the torque, i.e., $\hat{T}^- = \hat{T}^x - i\hat{T}^y$. Using Lehmann representation [40], we rewrite the Bloch eigenstates by Green's function \mathcal{G} , and define the spectral function $\hat{A} = i(\mathcal{G}^R - \mathcal{G}^A)$ with the retarded (R) and advanced (A) Green's function,

$$\alpha^{\mu\nu}(\mathbf{q}) = \frac{g}{m_s\pi} \text{Tr} \int_{\Omega} \eta(\varepsilon) \hat{T}^{\mu} \hat{A}(\hat{T}^{\nu})^{\dagger} \hat{A}_{\mathbf{k}+\mathbf{q}} d\mathbf{k} d\varepsilon. \quad (3)$$

The Fourier transformation of the Green's function \mathcal{G} finally is used to obtain the nonlocal Gilbert damping tensor [23] between site i at position \mathbf{r}_i and site j at position \mathbf{r}_j ,

$$\alpha_{ij}^{\mu\nu} = \frac{g}{m_s\pi} \text{Tr} \int \eta(\varepsilon) \hat{T}_i^{\mu} \hat{A}_{ij}(\hat{T}_j^{\nu})^{\dagger} \hat{A}_{ji} d\varepsilon. \quad (4)$$

Note that $\hat{A}_{ij} = i(\mathcal{G}_{ij}^R - \mathcal{G}_{ji}^A)$. This result is consistent with the formulation given in Refs. [14,32]. Hence the definition of nonlocal damping in real space and reciprocal space translate into each other by a Fourier transformation:

$$\alpha_{ij} = \int \alpha(\mathbf{q}) e^{-i(\mathbf{r}_j - \mathbf{r}_i) \cdot \mathbf{q}} d\mathbf{q}. \quad (5)$$

Note the obvious advantage of using Eq. (4), since it allows for a direct calculation of α_{ij} , as opposed to taking the inverse Fourier transform of Eq. (5). We would like to emphasize that \mathbf{q} refers to a particular wave vector, however, the underlying magnetic state is ferromagnetic. The dependency on the magnetic configuration, as discussed in Ref. [27], is neglected. Consequently, a direct comparison to experiment [29–31] is not straightforward.

For first-principles studies, the Green's function is obtained from a tight-binding (TB) model based on the Slater-Koster parametrization [41]. The Hamiltonian consists of on-site potentials, hopping terms, Zeeman energy, and spin-orbit coupling (see Appendix A). The TB parameters, including the spin-orbit coupling strength, are obtained by fitting the TB band structures to *ab initio* band structures as reported elsewhere [23].

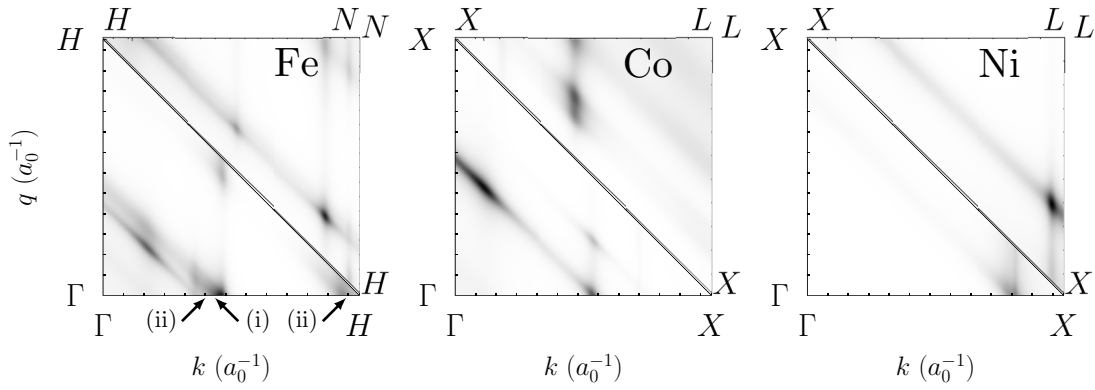


FIG. 2. Electronic state resolved nonlocal Gilbert damping obtained from the integrand of Eq. (3) along selected paths in the Brillouin zone for bcc Fe, fcc Co, and fcc Ni. The scattering rate used is $\Gamma = 0.01$ eV. The abscissa (both top and bottom in each panels) shows the momentum path of the electron \mathbf{k} , where the ordinate (left and right in each panel) shows the magnon propagation vector \mathbf{q} . The two “triangles” in each panel should be viewed separately where the magnon momentum changes accordingly (along the same path) to the electron momentum.

Beyond our model study, we simulate material specific nonlocal damping with the help of the full-potential linear muffin-tin orbitals (FP-LMTO) code RSPt [42,43]. Further numerical details are provided in Appendix A.

The above discussed Kamberský model is only applicable in certain, but established limits. (i) Time scales of the electron and spin degree-of-freedom have to be separable (adiabatic limit) to guarantee the validity of the magnetic force theorem. Rapid variations in time (e.g., at ultrafast demagnetization) or in space (e.g., nanodomain walls) do not properly equilibrate the electron-degree of freedom. (ii) The Kamberský model assumes a separation between the exchange and the spin-orbit part of the electron Hamiltonian that are discussed to cause precession and dissipation, respectively. This is in general not valid, since spin-orbit enters also into the precession field via anisotropic exchanges. This is handled within a generalized torque relation in Refs. [14,44]. (iii) The above model does not allocate the spectral width Γ to a particular mechanism (electron-phonon coupling, electron correlation, etc.) and, consequently, is a fitting parameter to the experiment.

With the aim to emphasize the importance of nonlocal Gilbert damping in the evolution of atomistic magnetic moments, we performed atomistic magnetization dynamics by numerically solving the Landau-Lifshitz-Gilbert (LLG) equation, explicitly incorporating nonlocal damping [23,35,45]

$$\frac{\partial \mathbf{m}_i}{\partial t} = \mathbf{m}_i \times \left(-\gamma \mathbf{B}_i^{\text{eff}} + \sum_j \frac{\alpha_{ij}}{m_s^j} \frac{\partial \mathbf{m}_j}{\partial t} \right). \quad (6)$$

Here, the effective field $\mathbf{B}_i^{\text{eff}} = -\partial \hat{H} / \partial \mathbf{m}_i$ is allocated to the spin Hamiltonian and entails Heisenberg-like exchange coupling $-\sum_{ij} J_{ij} \mathbf{m}_i \cdot \mathbf{m}_j$ and uniaxial magnetocrystalline anisotropy $\sum_i K_i (\mathbf{m}_i \cdot \mathbf{e}_i)^2$ with the easy axis along \mathbf{e}_i . J_{ij} and K_i are the Heisenberg exchange coupling and the magnetocrystalline anisotropy constant, respectively, and were obtained from first principles [46,47]. The dissipation term in Eq. (6) can be derived from a Lagrangian formalism with generalized Rayleigh dissipation functional, in a similar way as was already done in Ref. [48]. It remains still an open question if the dissipation term in Eq. (6) can be allocated to the dissipation

term of the micromagnetic Landau-Lifshitz-Bar equation [49], which is proportional to the $\nabla^2 \partial \mathbf{m}_i / \partial t$, where ∇ is the spatial gradient of the micromagnetic magnetic moment. Further details are provided in Appendix A.

III. RESULTS AND DISCUSSION

This section is divided in three parts. In the first part, we discuss nonlocal damping in reciprocal space \mathbf{q} . The second part deals with the real-space definition of the Gilbert damping α_{ij} . Atomistic magnetization dynamics including nonlocal Gilbert damping is studied in the third part.

A. Nonlocal damping in reciprocal space

The formalism derived by Kamberský [10] and Gilmore [12] in Eq. (2) represents the nonlocal contributions to the energy dissipation in the LLG equation by the magnon wave vector \mathbf{q} . In particular, Gilmore *et al.* [33] concluded that for transition metals at room temperature the single-mode damping rate is essentially independent of the magnon wave vector for \mathbf{q} between 0 and 1% of the Brillouin zone edge. However, for very small scattering rates Γ , Gilmore and Stiles [12] observed for bcc Fe, hcp Co, and fcc Ni a strong decay of α with \mathbf{q} , caused by the weighting function $W_{nm}(\mathbf{k}, \mathbf{k} + \mathbf{q})$ without any significant changes of the torque matrix elements. Within our model systems, we observed the same trend for bcc Fe, fcc Co, and fcc Ni. To understand the decay of the Gilbert damping with magnon wave vector \mathbf{q} in more detail, we study selected paths of both the magnon \mathbf{q} and electron momentum \mathbf{k} in the Brillouin zone at the Fermi energy ε_F for bcc Fe ($\mathbf{q}, \mathbf{k} \in \Gamma \rightarrow H$ and $\mathbf{q}, \mathbf{k} \in H \rightarrow N$), fcc Co, and fcc Ni ($\mathbf{q}, \mathbf{k} \in \Gamma \rightarrow X$ and $\mathbf{q}, \mathbf{k} \in X \rightarrow L$) [see Fig. 2 where the integrand of Eq. (2) is plotted]. For example, in Fe, a usually twofold degenerated d band [approximately in the middle of ΓH , marked by (i)] gives a significant contribution to the intraband damping for small scattering rates. There are two other contributions to the damping [marked by (ii)], that are caused purely by interband transitions. With increasing, but small \mathbf{q} the intensities of the peaks decrease and interband transitions become more likely. With larger \mathbf{q} , however, more and more interband transitions appear, which

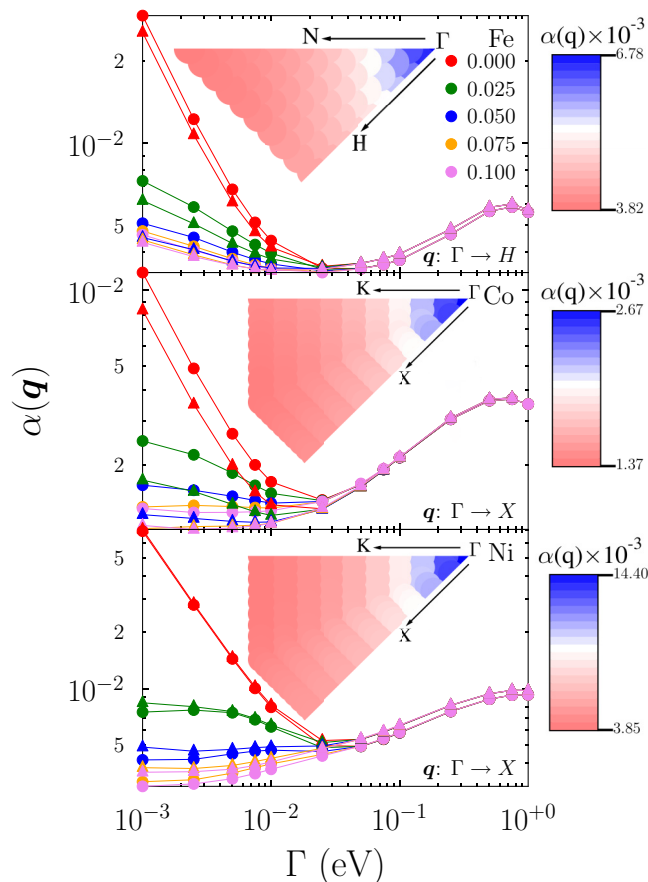


FIG. 3. Nonlocal Gilbert damping as a function of the spectral width Γ for different reciprocal wave vectors q (indicated by different colors and in units a_0^{-1}). Note that q provided here are in direct coordinates and only the direction differs between the different elemental, itinerant magnets. The nonlocal damping is shown for bcc Fe (top) along $\Gamma \rightarrow H$, for fcc Co (middle) along $\Gamma \rightarrow X$, and for fcc Ni (bottom) along $\Gamma \rightarrow X$. It is obtained from “Lorentzian” [Eq. (2), circles] and Green’s function [Eq. (3), triangles] method. The directional dependence of α for $\Gamma = 0.01$ eV is shown in the inset.

leads to an increase of the peak intensity, significantly in the peaks marked with (ii). This increase could be the same order of magnitude as the pure intraband transition peak. Similar trends also occur in Co as well as Ni and are also observed for Fe along the path \overline{HN} . Larger spectral width Γ increases the interband spin-flip transitions even further (data not shown). Note that the torque-torque correlation model might fail for large values of q , since the magnetic moments change so rapidly in space that the adiabatic limit is violated [50] and electrons are not stationary equilibrated. The electrons do not align according the magnetic moment and the nonequilibrium electron distribution in Eq. (2) will not fully relax. In particular, the magnetic force theorem used to derive Eq. (3) may not be valid.

The integration of the contributions in electron momentum space k over the whole Brillouin zone is presented in Fig. 3, where both “Lorentzian” method given by Eq. (2) and Green’s function method represented by Eq. (3) are applied. Both methods give the same trend, however, differ slightly in the

intraband region, which was already observed previously by the authors of Ref. [23]. In the Lorentzian approach, Eq. (2), the electronic structure itself is unaffected by the scattering rate Γ , only the width of the Lorentzian used to approximate A_{nk} is affected. In the Green function approach, however, Γ enters as the imaginary part of the energy at which the Green functions is evaluated and, consequently, broadens and shifts maxima in the spectral function. This offset from the real energy axis provides a more accurate description with respect to the *ab initio* results than the Lorentzian approach.

Within the limits of our simplified electronic structure tight-binding method, we obtained qualitatively similar trends as observed by Gilmore *et al.* [33]: a dramatic decrease in the damping at low scattering rates Γ (intraband region). This trend is common for all here observed itinerant magnets typically in a narrow region $0 < |q| < 0.02a_0^{-1}$, but also for different magnon propagation directions. For larger $|q| > 0.02a_0^{-1}$, the damping could again increase (not shown here). The decay of α is only observable below a certain threshold scattering rate Γ , typically where intra- and interband terms are equally contributing to the Gilbert damping. As already found by Gilmore *et al.* [33] and Thonig *et al.* [23], this point is materials specific. In the interband regime, however, damping is independent of the magnon propagator, caused by already allowed transitions between the electron bands due to band broadening. Marginal variations in the decay with respect to the direction of q (inset of Fig. 3) are revealed, which was not reported before. Such behavior is caused by the break of the space group symmetry due to spin-orbit coupling and a selected global spin-quantization axis along z direction, but also due to the noncubic symmetry of \mathcal{G}_k for $k \neq 0$. As a result, e.g., in Ni, the nonlocal damping decays faster along $\overline{\Gamma K}$ than in $\overline{\Gamma X}$. This will be discussed more in detail in the next section. An experimental verification of these results might be possible following the setup in Ref. [31], however, for arbitrary wave vectors (larger mode number) and bulk materials.

We also investigated the scaling of the nonlocal Gilbert damping with respect to the spin-orbit coupling strength ξ_d of the d states (see Appendix B). We observe an effect that previously has not been discussed, namely that the nonlocal damping has a different exponential scaling with respect to the spin-orbit coupling constant for different $|q|$. In the case where q is close to the Brillouin zone center (in particular $q = 0$), $\alpha \propto \xi_d^3$, whereas for wave vectors $|q| > 0.02a_0^{-1}$, $\alpha \propto \xi_d^2$. For large q , typically interband transitions dominate the scattering mechanism, as we show above and which is known to scale proportional to ξ^2 . Here, in particular, the ξ^2 will be caused only by the torque operator in Eq. (2). On the other hand, this indicates that spin-mixing transitions become less important because there is not contribution in ξ from the spectral function entering the damping $\alpha(q)$.

The validity of the Kambserky model becomes arguable for ξ^3 scaling, as it was already proved by Costa *et al.* [51] and Edwards [52], since it causes an unphysical and strong diverging intraband contribution at very low temperature (small Γ). Note that there is no experimental evidence of such a trend, most likely due to that sample impurities also influence Γ . Furthermore, various other methods postulate that the Gilbert damping for $q = 0$ scales like ξ^2 [9,15,22].

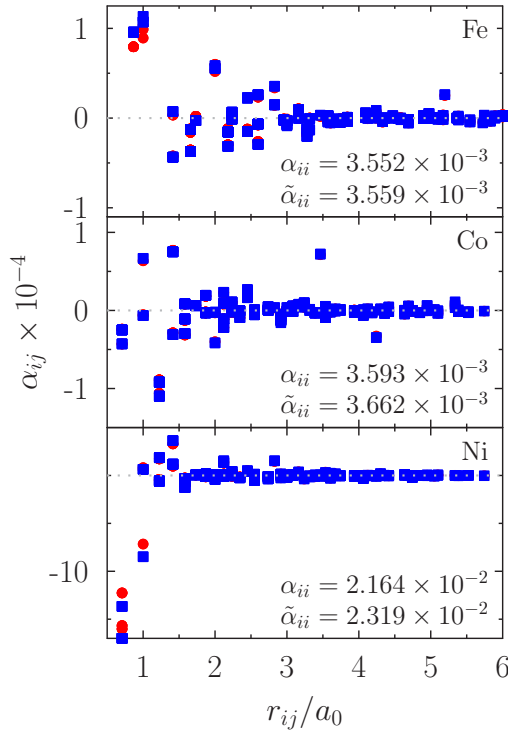


FIG. 4. Real-space Gilbert damping α_{ij} as a function of the distance r_{ij} between two sites i and j for bcc Fe, fcc Co, and fcc Ni. Both the “corrected” Kamberský (red circles) and the Kamberský (blue squares) approach is considered. The distance is normalized to the lattice constant a_0 . The on-site damping α_{ii} is shown in the figure label. The grey dotted line indicates the zero line. The spectral width is $\Gamma = 0.005$ eV.

Hence the current applied theory, Eq. (3), seems to be valid only in the long-wave limit, where we found ξ^2 scaling. On the other hand, Edwards [52] proved that the long-wavelength limit (ξ^2 scaling) holds also in the short-range limit if one accounts only for transitions that conserve the spin (“pure” spin states), as we show for Co in Fig. 11 of Appendix C. The trend α versus $|\mathbf{q}|$ as described above changes drastically for the “corrected” Kamberský formula: the interband region is not affected by these corrections. In the intraband region, however, the divergent behavior of α disappears and the Gilbert damping monotonically increases with larger magnon wave vector and over the whole Brillouin zone. This trend is in good agreement with Ref. [29]. For the case where $\mathbf{q} = 0$, we even reproduced the results reported in Ref. [21]; in the limit of small scattering rates, the damping is constant, which was also reported before in experiment [53,54]. Furthermore, the anisotropy of $\alpha(\mathbf{q})$ with respect to the direction of \mathbf{q} (as discussed for the insets of Fig. 3) increases by accounting only for pure-spin states (not shown here). Both agreement with experiment and previous theory motivate to consider ξ^2 scaling for all Γ .

B. Nonlocal damping in real space

Atomistic spin-dynamics, as stated in Sec. II [see Eq. (6)], which includes nonlocal damping, requires Gilbert damping in real space, e.g., in the form α_{ij} . This point is addressed in this section. Such nonlocal contributions are not excluded in the

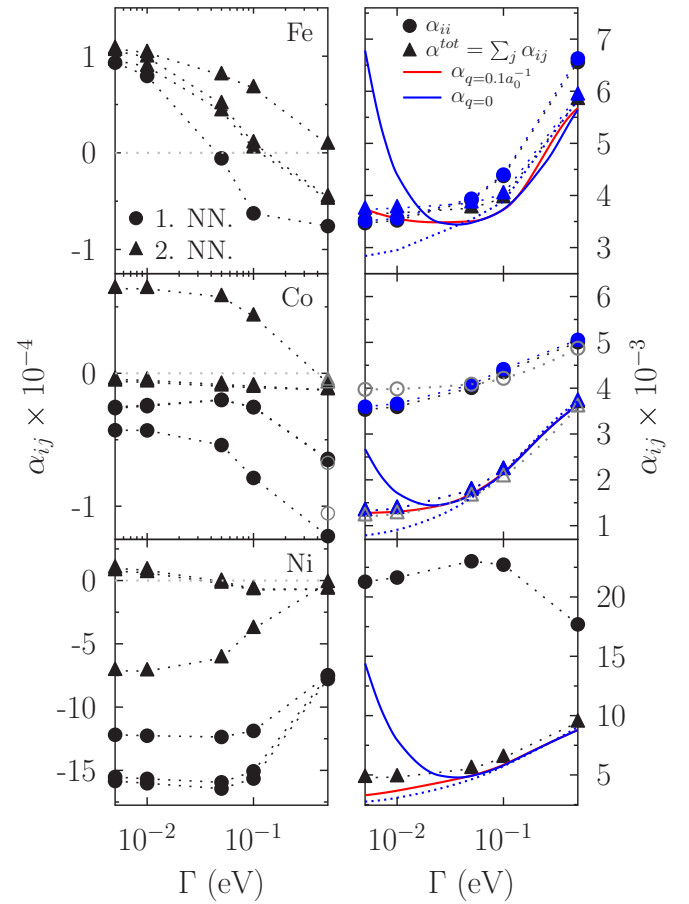


FIG. 5. First (circles) and second-nearest-neighbor (triangles) Gilbert damping (left) as well as on-site (circles) and total (triangles) Gilbert damping (right) as a function of the spectral width Γ for the itinerant magnets Fe, Co, and Ni. In particular for Co, the results obtained from tight binding are compared with first-principles density functional theory results (gray open circles). Solid lines (right panel) show the Gilbert damping obtained for the magnon wave vectors $q = 0$ (blue line) and $q = 0.1a_0^{-1}$ (red line). Dotted lines are added to guide the eye. Note that since cubic symmetry is broken (see text), there are two sets of nearest-neighbor parameters and two sets of next nearest-neighbor parameters (left panel) for any choice of Γ .

Rayleigh dissipation functional, applied by Gilbert to derive the dissipation contribution in the equation of motion [48] (see Fig. 4).

Dissipation is dominated by the on-site contribution α_{ii} in the itinerant magnets investigated here. For both Fe ($\alpha_{ii} = 3.55 \times 10^{-3}$) and Co ($\alpha_{ii} = 3.59 \times 10^{-3}$), the on-site damping contribution is similar, whereas for Ni α_{ii} is one order of magnitude higher. Off-site contributions $i \neq j$ are one order of magnitude smaller than the on-site part and can be even negative. Such negative damping is discernible also in Ref. [55], however, it was not further addressed by the authors. Due to the presence of the spin-orbit coupling and a preferred global spin-quantization axis (in z direction), the cubic symmetry of the considered itinerant magnets is broken and, thus, the Gilbert damping is anisotropic with respect to the sites j (see also Fig. 5 left panel). For example, in Co, four of the in-plane nearest neighbors (NN) are $\alpha_{\text{NN}} \approx -4.3 \times 10^{-5}$, while the other eight

are $\alpha_{\text{NN}} \approx -2.5 \times 10^{-5}$. However, in Ni, the trend is opposite: the out-of-plane damping ($\alpha_{\text{NN}} \approx -1.6 \times 10^{-3}$) is smaller than the in-plane damping ($\alpha_{\text{NN}} \approx -1.2 \times 10^{-3}$). Involving more neighbors, the magnitude of the nonlocal damping is found to decay as $1/r^2$ and, consequently, it is different than the Heisenberg exchange parameter that asymptotically decays in RKKY-fashion as $J_{ij} \propto 1/r^3$ [56]. For the Heisenberg exchange, the two Green's functions as well as the energy integration in the Lichtenstein-Katsnelson-Antropov-Gubanov formula [57] scales like r_{ij}^{-1} ,

$$\mathcal{G}_{ij}^{\sigma} \propto \frac{e^{i(\mathbf{k}^{\sigma} \cdot \mathbf{r}_{ij} + \Phi^{\sigma})}}{|\mathbf{r}_{ij}|}, \quad (7)$$

whereas for simplicity we consider here a single-band model but the results can be generalized also to the multiband case and where Φ^{σ} denotes a phase factor for spin $\sigma = \uparrow, \downarrow$. For the nonlocal damping, the energy integration is omitted due to the properties of η in Eq. (4) and, thus,

$$\alpha_{ij} \propto \frac{\sin(\mathbf{k}^{\uparrow} \cdot \mathbf{r}_{ij} + \Phi^{\uparrow}) \sin(\mathbf{k}^{\downarrow} \cdot \mathbf{r}_{ij} + \Phi^{\downarrow})}{|\mathbf{r}_{ij}|^2}. \quad (8)$$

This spatial dependency of α_{ij} superimposed with Ruderman-Kittel-Kasuya-Yosida (RKKY) oscillations was also found in Ref. [55] for a model system.

For Ni, dissipation is very much short range, whereas in Fe and Co “damping peaks” also occur at larger distances (e.g., for Fe at $r_{ij} = 5.1a_0$ and for Co at $r_{ij} = 3.4a_0$). The “long-rangeness” depends strongly on the parameter Γ (not shown here). As it was already observed for the Heisenberg exchange interaction J_{ij} [46], stronger thermal effects represented by Γ will reduce the correlation length between two magnetic moments at site i and j . The same trend is observed for damping: larger Γ causes smaller dissipation correlation length and, thus, a faster decay of nonlocal damping in space r_{ij} . Different from the Heisenberg exchange, the absolute value of the nonlocal damping typically decreases with Γ as it is demonstrated in Fig. 5.

Note that the change of the magnetic moment length is not considered in the results discussed so far. The anisotropy with respect to the sites i and j of the nonlocal Gilbert damping continues in the whole range of the scattering rate Γ and is controlled by it. For instance, the second-nearest-neighbors damping in Co and Ni become degenerated at $\Gamma = 0.5$ eV, where the anisotropy between first-nearest-neighbor sites increases. Our results show also that the sign of α_{ij} is affected by Γ (as shown in Fig. 5 left panel). Controlling the broadening of Bloch spectral functions Γ is in principle possible to evaluate from theory, but more importantly it is accessible from experimental probes such as angular-resolved photoelectron spectroscopy and two-photon electron spectroscopy.

The importance of nonlocality in the Gilbert damping depends strongly on the material (as shown in Fig. 5 right panel). It is important to note that the total—defined as $\alpha^{\text{tot}} = \sum_j \alpha_{ij}$ for arbitrary i —but also the local ($i = j$) and the nonlocal ($i \neq j$) part of the Gilbert damping do not violate the thermodynamic principles by gaining angular momentum (negative total damping). For Fe, the local and total damping are comparable in the whole range of Γ and, thus, the nonlocal

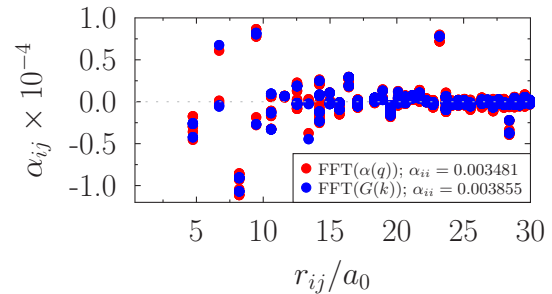


FIG. 6. Comparing nonlocal Gilbert damping obtained by Eq. (5) (red symbols) and Eq. (4) (blue symbols) in fcc Co for $\Gamma = 0.005$ eV. The dotted line indicates zero value.

contribution is negligible small. However in Co and Ni, local and total damping are significantly different revealing an important nonlocal damping contribution. The trends coming from our tight-binding electron structure were also reproduced by our all-electron first-principles simulation, for both dependency on the spectral broadening Γ (Fig. 5, gray open circles) but also site resolved nonlocal damping in the intraband region (see Appendix A), in particular, for fcc Co.

A direct experimental observation of α_{ij} might be not possible, however, magnon lifetimes could be measured as a function of the wave vector \mathbf{q} , as was done in Ref. [31], or by analyzing switching processes that include a noncollinear intermediate state. These magnon lifetimes could be, e.g., fitted to an effective model including nearest-neighbor nonlocal damping. Such a procedure is already established for magnetic exchange [58].

We compare also the nonlocal damping obtain from the real and reciprocal space. For this, we used Eq. (3) by simulating $N_q = 15 \times 15 \times 15$ points in the first magnon Brillouin zone \mathbf{q} and Fourier transformed it (Fig. 6). For both approaches, we obtain good agreement, corroborating our methodology and possible applications in both spaces. The nonlocal damping for the first three nearest-neighbor shells turn out to converge rapidly with N_q , while it does not converge so quickly for larger distances r_{ij} . The critical region around the Γ point in the Brillouin zone is suppressed in the integration over \mathbf{q} . On the other hand, the relation $\alpha^{\text{tot}} = \sum_j \alpha_{ij} = \alpha(q = 0)$ for arbitrary i should be valid, which is, however, violated in the intraband region as shown in Fig. 5 (compare triangles and blue line in Fig. 5): the real-space damping is constant for small Γ and follows the long-wavelength limit (compare triangles and red line in Fig. 5) rather than the divergent ferromagnetic mode ($q = 0$). Two explanations are possible: (i) convergence with respect to the real-space summation and (ii) a different scaling in both models with respect to the spin-orbit coupling. For (i), we carefully checked the convergence with the summation cutoff (see Appendix D) and found even a lowering of the total damping for larger cutoff. However, the nonlocal damping is very long-range and, consequently, convergence will be achieved only at a cutoff radius $\gg 9a_0$.

For (ii), we checked the scaling of the real-space Gilbert damping with the spin-orbit coupling of the d states (see Appendix B). Opposite to the “noncorrected” Kamberský formula in reciprocal space, which scales like ξ_d^3 , we find ξ_d^2 for the real-space damping. This indicates that the spin-flip scattering

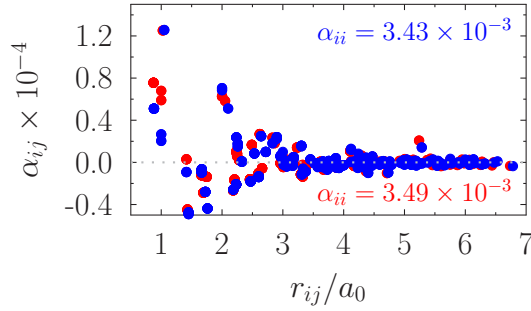


FIG. 7. Nonlocal Gilbert damping as a function of the normalized distance r_{ij}/a_0 for a tetragonal distorted bcc Fe crystal structure. Here, $c/a = 1.025$ (red circles) and $c/a = 1.05$ (blue circles) is considered. Γ is put to 0.01 eV. The zero value is indicated by dotted lines.

hosted in the real-space Green’s function is suppressed. To corroborate this statement further, we applied the corrections proposed by Edwards [52] to our real-space formula (4), which by default assumes ξ^2 (Fig. 4, red dots). Both methods, corrected and noncorrected Eq. (4), agree quite well. The small discrepancies are due to increased hybridizations and band inversion between p and d states due to spin-orbit coupling in the noncorrected case.

Finally, we address other ways than temperature (here represented by Γ) to manipulate the nonlocal damping. It is well established in literature already for Heisenberg exchange and the magnetocrystalline anisotropy that compressive or tensile strain can be used to tune the magnetic phase stability and to design multiferroic materials. In an analogous way, also nonlocal damping depends on distortions in the crystal (see Fig. 7).

Here, we applied nonvolume conserved tetragonal strain along the c axis. The local damping α_{ii} is marginally biased. Relative to the values of the undistorted case, a stronger effect is observed for the nonlocal part, in particular for the first few neighbors. Since we do a nonvolume conserved distortion, the in-plane second-NN component of the nonlocal damping is constant. The damping is in general decreasing with increasing distortion, however, a change in the sign of the damping can also occur (e.g., for the third NN). The rate of change in damping is not linear. In particular, the nearest-neighbor rate is about $\delta\alpha \approx 0.4 \times 10^{-5}$ for 2.5% distortion, and 2.9×10^{-5} for 5% from the undistorted case. For the second-nearest-neighbor, the rate is even bigger (3.0×10^{-5} for 2.5%, 6.9×10^{-5} for 5%). For neighbors larger than $r_{ij} = 3a_0$, the change is less significant (-0.6×10^{-5} for 2.5%, -0.7×10^{-5} for 5%). The strongly strain-dependent damping motivates even higher-order coupled damping contributions obtained from Taylor expanding the damping contribution around the equilibrium position α_{ij}^0 : $\alpha_{ij} = \alpha_{ij}^0 + \partial\alpha_{ij}/\partial\mathbf{u}_k \cdot \mathbf{u}_k + \dots$. Note that this is in analogy to the magnetic exchange interaction [59] (exchange striction) and a natural name for it would be “dissipation striction.” This opens new ways to dissipatively couple spin and lattice reservoir in combined dynamics [59], to the best of our knowledge not considered in today’s *ab initio* modeling of atomistic magnetization dynamics.

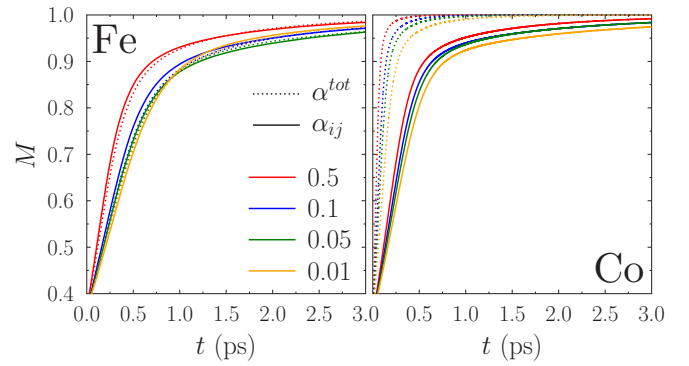


FIG. 8. Evolution of the average magnetic moment M during remagnetization in bcc Fe (left) and fcc Co (right) for different damping strength according to the spectral width Γ (different colors) and both, full nonlocal α_{ij} (solid line) and total, purely local α^{tot} (dashed line) Gilbert damping.

C. Atomistic magnetization dynamics

The question about the importance of nonlocal damping in atomistic magnetization dynamics (ASD) remains. For this purpose, we performed zero-temperature ASD for bcc Fe and fcc Co bulk and analysed changes in the average magnetization during relaxation from a totally random magnetic configuration, for which the total moment was zero (Fig. 8).

Related to the spectral width, the velocity for remagnetisation changes and is higher, the bigger the effective Gilbert damping is. For comparison, we performed also ASD simulations based on Eq. (2) with a scalar, purely local damping α^{tot} (dotted lines). For Fe, it turned out that accounting for the nonlocal damping causes a slight decrease in the remagnetization time, however, is overall not important for relaxation processes. This is understandable by comparing the particular damping values in Fig. 5, right panel, in which the nonlocal part appear negligible. On the other hand, for Co, the effect on the relaxation process is much more significant, since the nonlocal Gilbert damping reduces the local contribution drastically (see Fig. 5, right panel). This “negative” nonlocal part ($i \neq j$) in α_{ij} decelerates the relaxation process and the relaxation time is drastically increased by a factor of 10. Note that a “positive” nonlocal part will accelerate the relaxation, which is of high interest for ultrafast switching processes.

IV. CONCLUDING REMARKS

In conclusion, we have evaluated the nonlocality of the Gilbert damping parameter in both reciprocal and real space for elemental, itinerant magnets bcc Fe, fcc Co, and fcc Ni. In particular, in the reciprocal space, our results are in good agreement with values given in the literature [33]. The here studied real-space damping was considered on an atomistic level and it motivates to account for the full, nonlocal Gilbert damping in magnetization dynamic, e.g., at surfaces [60] or for nanostructures [61]. We revealed that nonlocal damping can be negative, has a spatial anisotropy, quadratically scales with spin-orbit coupling, and decays in space as r_{ij}^{-2} . Detailed comparison between real and reciprocal states identified the importance of the corrections proposed by Edwards [52] and,

consequently, overcome the limits of the Kamberský formula showing an unphysical and experimental not proved divergent behavior at low temperature. We further promote ways of manipulating nonlocal Gilbert damping, either by temperature, materials doping or strain, and motivating “dissipation striction” terms, that opens a fundamental new root in the coupling between spin and lattice reservoirs.

Our studies are the starting point for even further investigations: although we mimic temperature by the spectral broadening Γ , a precise mapping of Γ to spin and phonon temperature is still missing, according to Refs. [14,23]. Even at zero temperature, we revealed a significant effect of the non-local Gilbert damping to the magnetization dynamics, but the influence of nonlocal damping to finite temperature analysis or even to low-dimensional structures has to be demonstrated.

In analogy to the equivalence between the atomistic Heisenberg exchange and the micromagnetic exchange stiffness, the atomistic nonlocal damping should be carried over to a micromagnetic quantity. It turns out that it will lead to dissipation terms proportional to $\nabla \dot{\mathbf{m}}$ and $\nabla^2 \dot{\mathbf{m}}$, similar to dissipation terms entering to the Landau-Lifshitz-Bar equation [49,62,63]. However, a conceptual proof is still missing but this is out of the scope of the current manuscript although it is the main topic of an upcoming paper.

ACKNOWLEDGMENTS

The authors thank Lars Bergqvist, Lars Nordström, Justin Shaw, and Jonas Fransson for fruitful discussions. O.E. acknowledges the support from Swedish Research Council (VR), eSSSENCE, and the KAW Foundation (Grants No. 2012.0031 and No. 2013.0020). The computer simulations were performed on resources provided by the Swedish National Infrastructure for Computing (SNIC).

APPENDIX A: NUMERICAL DETAILS

We perform \mathbf{k} integration with up to 1.25×10^6 mesh points ($500 \times 500 \times 500$) in the first Brillouin zone for bulk. The energy integration is evaluated at the Fermi level only. For our first-principles studies, we performed a Slater-Koster parameterized [41] tight-binding (TB) calculation [64] of the torque-torque correlation model as well as for the Green’s function model. Here, the TB parameters have been obtained by fitting the electronic structures to those of a first-principles fully relativistic multiple scattering Korringa-Kohn-Rostoker (KKR) method using a genetic algorithm. The details of the fitting and the tight-binding parameters are listed elsewhere [23,65]. This puts our model on a firm, first-principles ground.

The tight-binding Hamiltonian [66] $\mathcal{H} = \mathcal{H}_0 + \mathcal{H}_{\text{mag}} + \mathcal{H}_{\text{soc}}$ contains on-site energies and hopping elements \mathcal{H}_0 , the spin-orbit coupling $\mathcal{H}_{\text{soc}} = \zeta \mathbf{S} \cdot \mathbf{L}$, and the Zeeman term $\mathcal{H}_{\text{mag}} = 1/2 \mathbf{B} \cdot \boldsymbol{\sigma}$. The Green’s function is obtained by $\mathcal{G} = (\varepsilon + i\Gamma - \mathcal{H})^{-1}$, which allows in principle to consider disorder in terms of spin and phonon as well as alloys [23]. The bulk Greenian \mathcal{G}_{ij} in real space between sites i and j is obtained by Fourier transformation. Despite the fact that the tight-binding approach is limited in accuracy, it produces good agreement with first-principles band structure calculations for energies smaller than $\varepsilon_F + 5 \text{ eV}$.

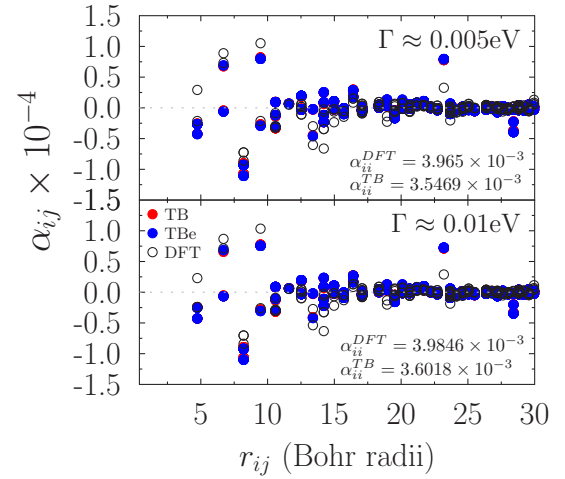


FIG. 9. Comparison of nonlocal damping obtained from the tight-binding method (TB) (red filled symbols), tight-binding with Edwards correction (TBe) (blue filled symbols), and the linear muffin-tin orbital method (DFT) (open symbols) for fcc Co. Two different spectral broadenings are chosen.

Equation (4) was also evaluated within the DFT and linear muffin-tin orbital method (LMTO) based code RSPT. The calculations were done for a k -point mesh of 128^3 k -points. We used three types of basis functions, characterized by different kinetic energies with $\kappa^2 = 0.1, -0.8, \text{ and } -1.7 \text{ Ry}$ to describe $4s, 4p, \text{ and } 3d$ states. The damping constants were calculated between the $3d$ orbitals, obtained using the muffin-tin head projection scheme [67]. Both the first-principles and tight-binding implementations of the nonlocal Gilbert damping agree well (see Fig. 9).

Note that due to numerical reasons, the values of Γ used for the comparisons are slightly different in both electronic structure methods. Furthermore, in the LMTO method, the orbitals are projected to d orbitals only, which leads to small discrepancies in the damping.

The atomistic magnetization dynamics is also performed within the CAHMD simulation package [64]. To reproduce bulk properties, periodic boundary conditions and a sufficiently large cluster ($10 \times 10 \times 10$) are employed. The numerical time step is $\Delta t = 0.1 \text{ fs}$. The exchange coupling constants J_{ij} are obtained from the Liechtenstein-Katsnelson-Antropov-Gubanov (LKAG) formula implemented in the first-principles fully relativistic multiple scattering Korringa-Kohn-Rostoker (KKR) method [40]. On the other hand, the magnetocrystalline anisotropy is used as a fixed parameter with $K = 50 \mu\text{eV}$.

APPENDIX B: SPIN-ORBIT COUPLING SCALING IN REAL AND RECIPROCAL SPACE

Kamberský’s formula is valid only for quadratic spin-orbit coupling scaling [21,51], which implies only scattering between states that preserve the spin. This mechanism was explicitly accounted by Edwards [52] by neglecting the spin-orbit coupling contribution in the “host” Green’s function. It is predicted for the coherent mode ($\mathbf{q} = 0$) [21] that this overcomes the unphysical and not experimentally verified

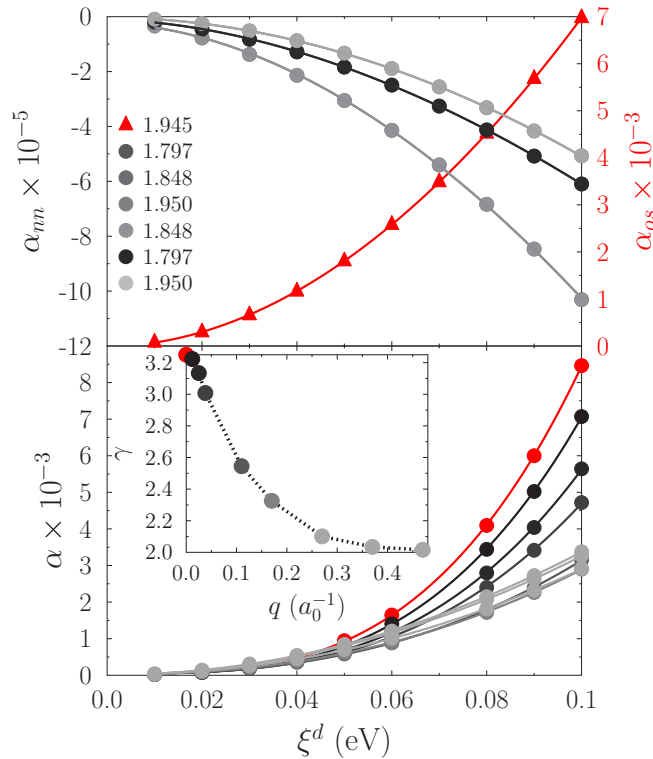


FIG. 10. Gilbert damping α as a function of the spin-orbit coupling for the d states in fcc Co. Lower panel shows the Gilbert damping in reciprocal space for different $\mathbf{q} = |\mathbf{q}|$ values (the color scheme used, represents different \mathbf{q} -values, as shown in the inset of the figure) along the $\Gamma \rightarrow X$ path. The upper panel exhibits the on-site α_{os} (red dots and lines) and nearest-neighbor α_{nn} (gray dots and lines) damping. The solid line is the exponential fit of the data point. The inset shows the fitted exponents γ with respect to wave vector q . The color of the dots is adjusted to the particular branch in the main figure. The spectral width is $\Gamma = 0.005$ eV.

divergent Gilbert damping for low temperature. Thus the methodology requires to prove the functional dependency of the (nonlocal) Gilbert damping with respect to the spin-orbit coupling constant ξ (Fig. 10). Since damping is a Fermi-surface effect, it is sufficient to consider only the spin-orbit coupling of the d states. The real-space Gilbert damping $\alpha_{ij} \propto \xi^\gamma$ scales for both on-site and nearest-neighbor sites with $\gamma \approx 2$. For the reciprocal space, however, the scaling is more complex and γ depends on the magnon wave vector \mathbf{q} (inset in Fig. 10). In the long-wavelength limit, the Kamberský formula is valid, where for the ferromagnetic magnon mode with $\gamma \approx 3$ the Kamberský formula is indefinite according to Edwards [52].

APPENDIX C: INTRABAND CORRECTIONS

For the same reason as discussed in Appendix B, the role of the correction proposed by Edwards [52] for magnon propagations different than zero is unclear and need to be studied. Hence we included the correction of Edward also to Eq. (3) (Fig. 11). The exclusion of the spin-orbit coupling (SOC) in the “host” clearly makes a major qualitative and quantitative change: although the interband transitions are unaffected, interband transitions are mainly suppressed, as

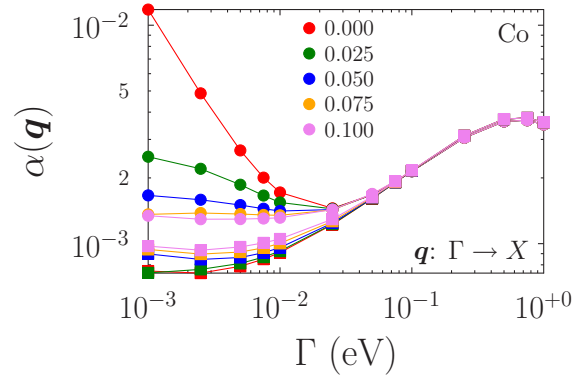


FIG. 11. Comparison of reciprocal nonlocal damping with (squares) or without (circles) corrections proposed by Costa *et al.* [51] and Edwards [52] for Co and different spectral broadening Γ . Different colors represent different magnon propagation vectors q .

it was already discussed by Barati *et al.* [21]. However, the intraband contributions are not totally removed for small Γ . For very small scattering rates, the damping is constant. Opposite to the noncorrected Kamberský formula, the increase of the magnon wave number \mathbf{q} gives an increase in the nonlocal damping, which is in agreement to the observation made by Yuan *et al.* [29], but also with the analytical model proposed in Ref. [55] for small \mathbf{q} . This behavior was observed for all itinerant magnets studied here.

APPENDIX D: COMPARISON REAL AND RECIPROCAL GILBERT DAMPING

The nonlocal damping scales like r_{ij}^{-2} with the distance between the sites i and j , and is, thus, very long-range. In order to compare $\alpha^{\text{tot}} = \sum_{j \in R_{\text{cut}}} \alpha_{ij}$ for arbitrary i with $\alpha(\mathbf{q} = 0)$, we have to specify the cutoff radius of the summation in real space (Fig. 12). The interband transitions ($\Gamma > 0.05$ eV) are already converged for small cutoff radii $R_{\text{cut}} = 3a_0$. Intraband transitions, on the other hand, converge weakly with R_{cut} to the reciprocal space value $\alpha(\mathbf{q} = 0)$. Note that $\alpha(\mathbf{q} = 0)$ is obtained from the corrected formalism. Even with $R_{\text{cut}} = 9a_0$, which is proportional to $\approx 30\,000$ atoms, we have not obtain convergence.

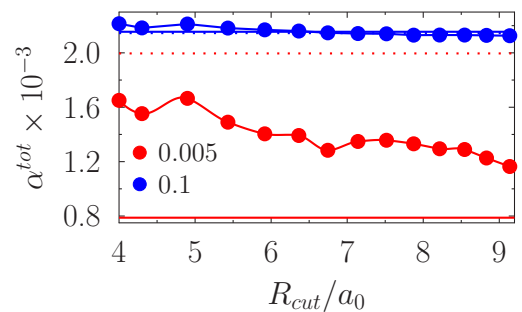


FIG. 12. Total Gilbert damping α^{tot} for fcc Co as a function of summation cutoff radius for two spectral widths Γ , one in the intraband ($\Gamma = 0.005$ eV, red dots and lines) and one in the interband ($\Gamma = 0.1$ eV, blue dots and lines) region. The dotted and solid lines indicate the reciprocal value $\alpha(\mathbf{q} = 0)$ with and without SOC corrections, respectively.

- [1] S. S. P. Parkin, M. Hayashi, and L. Thomas, *Science* **320**, 190 (2008).
- [2] J. Iwasaki, M. Mochizuki, and N. Nagaosa, *Nat. Nanotechnol.* **8**, 742 (2013).
- [3] A. Fert, V. Cros, and J. Sampaio, *Nat. Nanotechnol.* **8**, 152 (2013).
- [4] B. Behin-Aein, D. Datta, S. Salahuddin, and S. Datta, *Nat. Nanotechnol.* **5**, 266 (2010).
- [5] N. Locatelli, A. F. Vincent, A. Mizrahi, J. S. Friedman, D. Vodenicarevic, J.-V. Kim, J.-O. Klein, W. Zhao, J. Grollier, and D. Querlioz, in *DATE 2015* (IEEE Conference Publications, New Jersey, 2017), pp. 994–999.
- [6] K. Koumpouras, D. Yudin, C. Adelmann, A. Bergman, O. Eriksson, and M. Pereiro, [arXiv:1702.00579](https://arxiv.org/abs/1702.00579).
- [7] O. Eriksson, A. Bergman, L. Bergqvist, and J. Hellsvik, *Atomistic Spin Dynamics*, Foundations and Applications (Oxford University Press, Oxford, UK, 2016).
- [8] V. P. Antropov, M. I. Katsnelson, B. N. Harmon, M. van Schilfgaarde, and D. Kusnezov, *Phys. Rev. B* **54**, 1019 (1996).
- [9] V. Kamberský, *Phys. Rev. B* **76**, 134416 (2007).
- [10] V. Kamberský, *Czech. J. Phys.* **34**, 1111 (1984).
- [11] V. Kamberský, *Czech. J. Phys.* **26**, 1366 (1976).
- [12] K. Gilmore, Y. U. Idzerda, and M. D. Stiles, *Phys. Rev. Lett.* **99**, 027204 (2007).
- [13] A. A. Starikov, P. J. Kelly, A. Brataas, Y. Tserkovnyak, and G. E. W. Bauer, *Phys. Rev. Lett.* **105**, 236601 (2010).
- [14] H. Ebert, S. Mankovsky, D. Ködderitzsch, and P. J. Kelly, *Phys. Rev. Lett.* **107**, 066603 (2011).
- [15] S. Mankovsky, D. Ködderitzsch, G. Woltersdorf, and H. Ebert, *Phys. Rev. B* **87**, 014430 (2013).
- [16] M. A. W. Schoen, D. Thonig, M. L. Schneider, T. J. Silva, H. T. Nembach, O. Eriksson, O. Karis, and J. M. Shaw, *Nat. Phys.* **12**, 839 (2016).
- [17] J. Chico, S. Keshavarz, Y. Kvashnin, M. Pereiro, I. Di Marco, C. Etz, O. Eriksson, A. Bergman, and L. Bergqvist, *Phys. Rev. B* **93**, 214439 (2016).
- [18] P. Dürrenfeld, F. Gerhard, J. Chico, R. K. Dumas, M. Ranjbar, A. Bergman, L. Bergqvist, A. Delin, C. Gould, L. W. Molenkamp, and J. Åkerman, *Phys. Rev. B*, **92**, 214424 (2015).
- [19] M. A. W. Schoen, J. Lucassen, H. T. Nembach, T. J. Silva, B. Koopmans, C. H. Back, and J. M. Shaw, *Phys. Rev. B* **95**, 134410 (2017).
- [20] M. A. W. Schoen, J. Lucassen, H. T. Nembach, B. Koopmans, T. J. Silva, C. H. Back, and J. M. Shaw, *Phys. Rev. B* **95**, 134411 (2017).
- [21] E. Barati, M. Cinal, D. M. Edwards, and A. Umerski, *Phys. Rev. B* **90**, 014420 (2014).
- [22] F. Pan, J. Chico, J. Hellsvik, A. Delin, A. Bergman, and L. Bergqvist, *Phys. Rev. B* **94**, 214410 (2016).
- [23] D. Thonig and J. Henk, *New J. Phys.* **16**, 013032 (2014).
- [24] Z. Ma and D. G. Seiler, *Metrology and Diagnostic Techniques for Nanoelectronics* (Pan Stanford, Taylor & Francis Group, 6000 Broken Sound Parkway NW, Suite 300, Boca Raton, FL 33487-2742, 2017).
- [25] D. Steiauf and M. Fähnle, *Phys. Rev. B* **72**, 064450 (2005).
- [26] D. Thonig, J. Henk, and O. Eriksson, *Phys. Rev. B* **92**, 104403 (2015).
- [27] M. Fähnle and D. Steiauf, *Phys. Rev. B* **73**, 184427 (2006).
- [28] E. Minguzzi, *Eur. J. Phys.* **36**, 035014 (2015).
- [29] Z. Yuan, K. M. D. Hals, Y. Liu, A. A. Starikov, A. Brataas, and P. J. Kelly, *Phys. Rev. Lett.* **113**, 266603 (2014).
- [30] H. T. Nembach, J. M. Shaw, C. T. Boone, and T. J. Silva, *Phys. Rev. Lett.* **110**, 117201 (2013).
- [31] Y. Li and W. E. Bailey, *Phys. Rev. Lett.* **116**, 117602 (2016).
- [32] S. Bhattacharjee, L. Nordström, and J. Fransson, *Phys. Rev. Lett.* **108**, 057204 (2012).
- [33] K. Gilmore and M. D. Stiles, *Phys. Rev. B* **79**, 132407 (2009).
- [34] Kjetil Magne Dørheim Hals, A. K. Nguyen, and A. Brataas, *Phys. Rev. Lett.* **102**, 256601 (2009).
- [35] A. Brataas, Y. Tserkovnyak, and G. E. W. Bauer, *Phys. Rev. B* **84**, 054416 (2011).
- [36] R. Chimata, E. K. Delczeg-Czirjak, A. Szilva, R. Cardias, Y. O. Kvashnin, M. Pereiro, S. Mankovsky, H. Ebert, D. Thonig, B. Sanyal *et al.*, *Phys. Rev. B* **95**, 214417 (2017).
- [37] K. Gilmore, Ph.D. thesis, Montana State University, 2008 scholarworks.montana.edu.
- [38] K. Gilmore, I. Garate, A. H. MacDonald, and M. D. Stiles, *Phys. Rev. B* **84**, 224412 (2011).
- [39] M. Sayad, R. Rausch, and M. Potthoff, *Phys. Rev. Lett.* **117**, 127201 (2016).
- [40] J. Zabloudil, L. Szunyogh, R. Hammerling, and P. Weinberger, *Electron Scattering in Solid Matter, A Theoretical and Computational Treatise* (Springer, Berlin, 2006).
- [41] J. C. Slater and G. F. Koster, *Phys. Rev.* **94**, 1498 (1954).
- [42] J. M. Wills and B. R. Cooper, *Phys. Rev. B* **36**, 3809 (1987).
- [43] J. M. Wills, O. Eriksson, M. Alouani, and D. L. Price, in *Electronic Structure and Physical Properties of Solids*, edited by H. Dreyse (Springer Verlag, Berlin, 2000), p. 148; J. M. Wills, M. Alouani, P. Andersson, A. Delin, O. Eriksson, and A. Grechnev, in *Full-Potential Electronic Structure Method, Energy and Force Calculations with Density Functional and Dynamical Mean Field Theory*, Springer Series in Solid-State Sciences, Vol. 167 (2010).
- [44] F. Freimuth, S. Blügel, and Y. Mokrousov, *Phys. Rev. B* **96**, 104418 (2017).
- [45] C. Vittoria, S. D. Yoon, and A. Widom, *Phys. Rev. B* **81**, 014412 (2010).
- [46] D. Böttcher, A. Ernst, and J. Henk, *J. Magn. Magn. Mater.* **324**, 610 (2012).
- [47] A. Szilva, M. Costa, A. Bergman, L. Szunyogh, L. Nordström, and O. Eriksson, *Phys. Rev. Lett.* **111**, 127204 (2013).
- [48] T. L. Gilbert, *IEEE Trans. Magn.* **40**, 3443 (2004).
- [49] V. G. Baryakhtar, in *Frontiers in Magnetism of Reduced Dimension Systems* (Springer, Dordrecht, Dordrecht, 1998), pp. 63–94.
- [50] I. Garate, K. Gilmore, M. D. Stiles, and A. H. MacDonald, *Phys. Rev. B* **79**, 104416 (2009).
- [51] A. T. Costa and R. B. Muniz, *Phys. Rev. B* **92**, 014419 (2015).
- [52] D. M. Edwards, *J. Phys.: Condens. Matter* **28**, 086004 (2016).
- [53] M. Oogane, T. Wakitani, S. Yakata, R. Yilgin, Y. Ando, A. Sakuma, and T. Miyazaki, *Jpn. J. Appl. Phys.* **45**, 3889 (2006).
- [54] S. M. Bhagat and P. Lubitz, *Phys. Rev. B* **10**, 179 (1974).
- [55] N. Umetsu, D. Miura, and A. Sakuma, *J. Phys. Soc. Jpn.* **81**, 114716 (2012).
- [56] M. Pajda, J. Kudrnovský, I. Turek, V. Drchal, and P. Bruno, *Phys. Rev. B* **64**, 174402 (2001).
- [57] A. I. Liechtenstein, M. I. Katsnelson, V. P. Antropov, and V. A. Gubanov, *J. Magn. Magn. Mater.* **67**, 65 (1987).

- [58] J. Prokop, W. X. Tang, Y. Zhang, I. Tudosa, T. R. F. Peixoto, K. Zakeri, and J. Kirschner, *Phys. Rev. Lett.* **102**, 177206 (2009).
- [59] P.-W. Ma, S. L. Dudarev, and C. H. Woo, *Phys. Rev. B* **85**, 184301 (2012).
- [60] L. Bergqvist, A. Taroni, A. Bergman, C. Etz, and O. Eriksson, *Phys. Rev. B* **87**, 144401 (2013).
- [61] D. Böttcher, A. Ernst, and J. Henk, *J. Phys.: Condens. Matter* **23**, 296003 (2011).
- [62] V. G. Baryakhtar, *JETP* **60**, 863 (1984).
- [63] W. Wang, M. Dvornik, M.-A. Bisotti, D. Chernyshenko, M. Beg, M. Albert, A. Vansteenkiste, B. V. Waeyenberge, A. N. Kuchko, V. V. Kruglyak *et al.*, *Phys. Rev. B* **92**, 054430 (2015).
- [64] D. Thonig, *CAHMD- A Computer Program Package for Atomistic Magnetization Dynamics Simulations*, 2nd ed. (Uppsala University, Uppsala, 2013).
- [65] D. Thonig, O. Eriksson, and M. Pereiro, *Sci. Rep.* **7**, 931 (2017).
- [66] T. Schena, Ph.D. thesis, fz-juelich.de, 2010.
- [67] A. Grechnev, I. Di Marco, M. I. Katsnelson, A. I. Lichtenstein, J. Wills, and O. Eriksson, *Phys. Rev. B* **76**, 035107 (2007).